Lena Heuscher[1], Chuntao Liu[2], Patrick Gatlin[3], Walter A. Petersen[3]

[1] Department of Atmospheric and Earth Science, University of Alabama in Huntsville, Huntsville, Alabama, USA

[2] Department of Physical and Environmental Sciences, Texas A&M University at Corpus Christi, Corpus Christi, Texas, USA

[3] NASA Marshall Space Flight Center, Huntsville, Alabama, USA

Corresponding author: Lena Heuscher (lvh0002@uah.edu)

Key Points:

- GPM combined with GLM observations facilitates new investigations of convective precipitation in the mid-/high latitudes.
- Convective life cycle stage can be inferred by examining flash rate in terms of radar and passive microwave properties.
- Different synoptic environmental influences on observed precipitation/lightning properties are explained by impacts on physical processes.

Abstract

This study applies new satellite datasets and methodologies to build on previous research exploring the physical relationship between lightning and precipitation in mid-/high latitudes. Specifically, three years of Geostationary Lightning Mapper (GLM) and Global Precipitation Measurement (GPM) Mission core satellite coincident observations are examined to investigate relationships between lightning flash rate and microwave characteristics of convective precipitation features (cPFs) over the Americas and surrounding oceans between ± 50° latitude. Mid-/high latitude cPFs with lightning are characterized by colder temperatures of maximum 30 dBz echo top height and a smaller range of microwave brightness temperatures when compared to the tropics. Brightness temperature characteristics of electrically active cPFs are highly correlated to radar-diagnosed ice mass and largely insensitive to synoptic-scale proxies for convective strength and organization. Low flash density cPFs tend to be more sensitive to synoptic-scale instability and shear than high flash density cPFs. Regional differences in the environmental forcing and characteristics of electrically active cPFs are shown. For example, the elevated terrain surrounding the Amazon River Basin is characterized by stronger vertical updrafts indicated by higher values of normalized CAPE (NCAPE) while the La Plata River Basin is characterized by both stronger updrafts and higher values of radar-diagnosed ice water mass.

Plain Language Summary

New satellite-based lightning observations collected over Earth's mid-/high latitudes provide the opportunity to observe and better understand relationships between lightning and precipitation properties over a domain that significantly extends that of the historically better-sampled global tropics. Our research combines lightning data, continuously observed from the Geostationary Lightning

Mapper (GLM), with low-Earth orbiting precipitation "snapshots" collected from the Global Precipitation Measurement (GPM) Mission Core Observatory. Considered at hemispheric scales, the newly combined GPM and GLM observations suggest lightning and precipitation relationships derived from tropical observations also hold for the mid-/high latitudes. Regional nuances are found in the electrical and microwave characteristics of deep convection — mid-/high latitude convection is characterized by colder 30 dBz echo top heights and a smaller range of microwave brightness temperatures when compared to the tropics. Colder echo tops in the mid-/high latitudes indicate stronger updrafts than in the tropics. Large-scale environments where electrically-active convection is observed are also examined. Physical processes tied to deep convection (e.g., lofting of ice or updraft strength) can explain some trends in the satellite-observed precipitation and lightning data. Regional differences in the percentage of electrically active convection characterized by stronger inferred updrafts and higher derived values of ice are discussed.

1 Introduction

The Precipitation Radar (PR) onboard the Tropical Rainfall Measuring Mission (TRMM) satellite provided a rich legacy of data revealing the characteristics and climatologies of precipitation and its three dimensional structure spanning the latitudes of 36°N-36°S for over 17 years (e.g., Kummerow et al. 1998; Tao et al. 2006; Zipser et al. 2006; Huffman et al. 2007; Biasutti et al. 2012; Houze Jr. et al. 2015; Matsui et al. 2016). Over its lifetime, TRMM reinforced numerous previous, but more regional, observations suggesting that weaker and shallower convection tended to occur over oceans, while deeper and more intense convection was almost an exclusively over-land phenomenon. Coincidentally, more intense convection observed over landmasses produced significantly more lightning, as observed from the TRMM Lightning Imaging Sensor (LIS; e.g., Christian et al., 1999; Boccippio et al., 2000, 2005; Petersen & Rutledge, 2001; Zuluaga & Houze, 2015). This is no surprise since lightning activity is intimately linked to storm dynamics and ice-phase precipitation development (Workman & Reynolds, 1949; Saunders, 1993; Petersen & Rutledge, 2001; et al., 2005; Deierling & Petersen, 2008; Carey et al., 2019) and exhibits unique behavior in severe convective storms (Schultz et al. 2009; Gatlin and Goodman 2010; Schultz et al. 2011; Rudlosky and Fuelberg 2013). Paving the way for more in-depth statistical studies of storm "unit" physical properties responsible for correlated behavior between lightning and storm structure, TRMM PR, microwave radiometer (TMI), and coincident LIS data have been used to create precipitation feature (PF) databases (Liu et al. 2008).

The PF databases have proven useful for summarizing integrated storm-scale and dynamically-related tropical precipitation characteristics (e.g., Nesbitt et al. 2000; Cecil and Zipser 2002; Cecil et al. 2002; Toracinta et al. 2002; Liu et al. 2008, 2011, 2012). Of particular interest to this study are deep convective extreme storm indicators that include the following PF-based parameters: minimum 37- or 85-GHz polarization corrected brightness temperature (PCT;

Spencer et al. 1989; Cecil and Chronis 2018), maximum height of the 40 dBz echo top, and total lightning flash rate. Numerous studies have demonstrated that minimum PCT, especially at frequencies sensitive to ice scattering such as 37- and 85-GHz, can be used as a proxy for deeper, more vertically-developed convection as deeper convection tends to exhibit lower PCTs due to thicker layer of ice aloft (Wilheit et al. 1982; Wu & Weinman, 1984; Spencer et al 1989). Reflectivity can also be used as a metric for convective intensity, with increasing reflectivity values being the result of an increasing fraction of water and/or ice occupying the radar volume. When distributions of these different extreme storm indicators have been examined using TRMM data, results typically show that PFs with the lowest PCTs and tallest 40 dBz echoes have greater flash rates (Cecil et al. 2005; Liu et al. 2012).

While studies using TRMM data provided insight into tropical precipitation and lightning characteristics, its orbital inclination limited its view of higher latitude PFs. This is important because the large-scale dynamics and associated baroclinic cloud and precipitation systems that occur in the mid-latitudes are often very different from those found in the tropics (e.g., Lau & Crane, 1995). For example, mid-latitude cyclones consist of synoptic scale "conveyor belts" that drive warm air poleward and cold air towards the equator. As a result, spatially expansive, long-duration precipitation systems often exist around cyclone frontal zones, with associated vertical wind shear and large thermodynamic contrasts that facilitate organized convection capable of producing severe weather. There have yet to be any global scale analogue studies of the precipitation and lightning characteristics of such mid-/high latitude weather systems similar to those facilitated by TRMM (e.g., Nesbitt et al. 2000).

The Global Precipitation Measurement Mission (GPM; Hou et al., 2014) builds upon the TRMM legacy by providing new and closer-to-global satellite-based dual-frequency volumetric radar and microwave radiometer observations of precipitation in these previously under-sampled regions. For example, observations from the GPM mission have now well-demonstrated that intense precipitation systems with 40 dBz echoes extending above 10 km are frequently observed at mid-/high latitudes (Liu and Zipser 2015). The GPM core observatory has observed the expected presence of some of the most intense storm systems on Earth, over the Great Plains and Pampas regions of the US and Argentina respectively, both of which were not fully sampled during the TRMM mission. Adding considerable capability for the study and monitoring of global thunderstorm characteristics, development and deployment of Geostationary Lightning Mappers (GLMs; Goodman et al. 2013; Rudlosky et al. 2019), now flying on the GOES East and West satellites, provide temporally-continuous total lightning measurements covering the mid-/high latitudes to complement active and passive microwave observations collected from low Earth-orbiting (LEO) platforms such as GPM. The purpose of this study is to extend the TRMM record into the GPM era by incorporating GLM observations into the GPM PF database and use this new dataset to investigate precipitation and lightning characteristics of PFs in the mid-/high latitudes.

2 Dataset and Methodology

2.1 GLM

The GLM on the GOES-East (GOES-R in the series) satellite is the first lightning detection sensor in geostationary orbit and is extending the satellite-based lightning climatology provided by the TRMM LIS and earlier Optical Transient Detector (OTD; Christian et al. 2003) instruments over the western hemisphere (Goodman et al. 2013). The GLM is based on OTD and LIS heritage and uses a charge-coupled device imager with a focal plane that contains 1372 x 1300 pixels to detect optical pulses emitted by lightning in a narrow (~1-nm) spectral band centered at 777.4 nm. Its pixel size varies from ~8 km at nadir to ~14 km at the limb (Goodman et al. 2013). In this study, we use GLM flashes that, similar to LIS hierarchy, consist of sequential groups (i.e., simultaneous 2 ms events that exceed a detection threshold) separated by less than 330 ms and 16.5 km (Mach 2020). A recent evaluation of GOES-East GLM observations over Florida reveals an average GLM detection efficiency (DE) of 74% (88%) during the day (at night(Zhang and Cummins 2020). The GLM-DE can vary regionally or even on the storm-scale due to a combination of factors such as optical depth, satellite angle, and storm charge structure (Murphy and Said 2020; Rutledge et al. 2020).

In order to mitigate false alarms, degraded flash detection, and decreased data quality (e.g., sun glint, flash duration exceeding a threshold, flash event counts exceeding a threshold), only flashes with a quality flag = 0 are included in this study (Carlomusto 2019; Rudlosky et al. 2019; Rudlosky and Virts 2021). During the study time period (March 2018-April 2021), several noteworthy updates have been applied to the ground system software, which are linked to several observed artifacts in the GLM data. For more information on GLM processing updates and artifacts, readers are referred to Bateman and Mach (2020) and Rudlosky and Virts (2021).

2.2 GPM Precipitation Features (PFs) Database

The GPM mission consists of a LEO constellation of satellite-based microwave instruments to obtain a global map of precipitation on a 3-hourly temporal time scale (Hou et al. 2014). Anchoring this constellation as an on-orbit calibrator and laboratory, the GPM Core Observatory (GPM-CO) carries the first-spaceborne Dual-frequency Precipitation Radar (DPR), operating at the Ku (13.5 GHz) and Ka (35.5 GHz) bands, as well as a multi-channel (10-183 GHz) microwave imager (GMI; Hou et al. 2014). The GPM PFs are defined from DPR and GMI retrieval products similar to the approach used for the TRMM PF database (Liu et al. 2008). During this process, a GMI pixel is assigned to each DPR pixel using a nearest neighbor method. Next, a parallax correction is applied to account for differences in the inclination angle between the GMI (52°) and the DPR (cross-track scanning). This correction is only applied to pixels where the DPR-Ku echo top height is greater than 5 km and the path integrated attenuation is greater than 0.4 dBz in order to avoid an overcorrection for shal-

low precipitation. After the parallax correction, pixels are re-collocated to make the matching between the GMI and DPR more realistic (Liu 2016). PFs are then defined as contiguous pixels with a Ku-band radar-derived near-surface precipitation rate greater than 0.1 mm hr-1 (hereafter rPFs). Each pixel within a PF is classified by the DPR algorithm as stratiform, convective, or other (Iguchi et al., 2017) by evaluating both the vertical structure and horizontal texture of the Ku-band attenuation-corrected reflectivity field.

To focus on understanding convective precipitation, where the bulk of lightning occurs, convective PFs (cPFs) are defined by grouping the pixels with the convective precipitation classification; to align with GLM, we only consider rPFs and cPFs observed by GPM for a three-year period between March 2018 to April 2021, and over a latitude and longitude spatial domain spanning 50° N to 50°S and 134°W to 15°W, respectively. To reduce the possibility of non-precipitating echoes from DPR, only PFs larger than 4 pixels (~98 km^2) are considered in this study. Additional quality control includes removing features that are not fully within the DPR scan; this ensures that the entire PF is captured and the most intense part of the feature is not cut off by the scan edge. As relative trends before and after removing these PFs remain the same, all analysis is done with this removal in order to ensure the highest quality data, which reduces the rPF (cPF) dataset by 14.2% (8.5%) for a total sample size of 1,405,657 (1,039,022) features.

Within each rPF and cPF, properties are summarized from DPR and GMI observations, including geolocation and morphology (e.g., location, time, horizontal area, weighted ellipse fit, orientation), precipitation characteristics (e.g., volumetric precipitation/ice mass, maximum precipitation rate), vertical structure (e.g., maximum reflectivity profile in 500 m height bins, horizontal area with Ku-band reflectivity greater or equal to 20, 30, 40 dBz at 1 km height intervals), and convective intensity (e.g., minimum 37- and 89-GHz PCT, maximum 20 and 40 dBz echo top heights). Cold brightness temperatures at 37- and 89-GHz and high maximum heights of 30- and 40 dBz echoes have been used as proxies for intense convection with high lightning rates in the past (e.g., Cecil et al. 2005; Zipser et al. 2006; Liu et al. 2011, 2012); in order to latitudinally-normalize the physical processes in the vertical, the temperature of the maximum echo top heights are utilized instead of just using heights themselves. For the remainder of this study, minimum brightness temperatures (Tb) are denoted as $PCT_{channel}$ (e.g., PCT_{37GHz}). It should be noted that the Tb minima and maximum echo top heights represent the pixel extrema observed within a given PF. Additionally, there could be multiple discrete cells embedded within a larger precipitating system feature (e.g., mesoscale convective system, MCS), although some PFs may in fact be smaller isolated storms. The GPM PF database also includes several parameters from the fifth-generation European Centre for Medium-Range Weather Forecasts (ECMWF) global atmospheric reanalysis (ERA5; Hersbach et al. 2020) to provide large scale environmental context for the PFs (Liu 2016).

The ice water mass (IWM) for each PF is calculated by integrating the ice water

content for the feature's vertical profile within a given reflectivity threshold (e.g., 30 dBz) via:

$$\mathbf{IWM} = \mathbf{1000} \int_{\mathbf{-5^{\circ}C}}^{\mathbf{-35^{\circ}C}} \mathbf{1000}\ {}_{\mathbf{i}}\mathbf{N_0}^{\frac{\mathbf{3}}{\mathbf{7}}} \left(\frac{\mathbf{5.28x10^{-18}}}{\mathbf{720}}\mathbf{Z}\right)^{\frac{\mathbf{4}}{\mathbf{7}}} \mathrm{dV\ kg} \quad (1)$$

where $N_0 = 4 \times 10^6$ m^{-4} and $_i = 917$ kg m^{-3} (Carey and Rutledge 2000; Petersen and Rutledge 2001). Note that we apply this IWM relationship with caution as this reflectivity-mass (Z-M) relationship is defined for tropical convection, can vary significantly between storms, and GPM/GLM combined observations include mid-/high latitudes where the assumptions for this Z-M relationship may not always be valid.

2.3 Combining GPM PFs with lightning observations

GLM flashes from March 2018-April 2021 were collocated temporally and spatially with PFs observed by GPM within the GLM field of view (FOV). To account for PF evolution, a flash is assigned to a PF if it is within the PF ellipsoid and within a ±10-minute window centered on the GPM overpass time (Figure 1). If two PFs are adjacent, there is a possibility that GLM flashes may be assigned to multiple PFs. Analysis indicates that less than 2% of cPFs have overlapping ellipsoids. To avoid assignments of the same flash to multiple PFs, each GLM flash is assigned to the first PF (in time) it is identified with and for which the spatial and temporal constraints are satisfied (e.g., within the PF ellipse and the ±10-minute window).

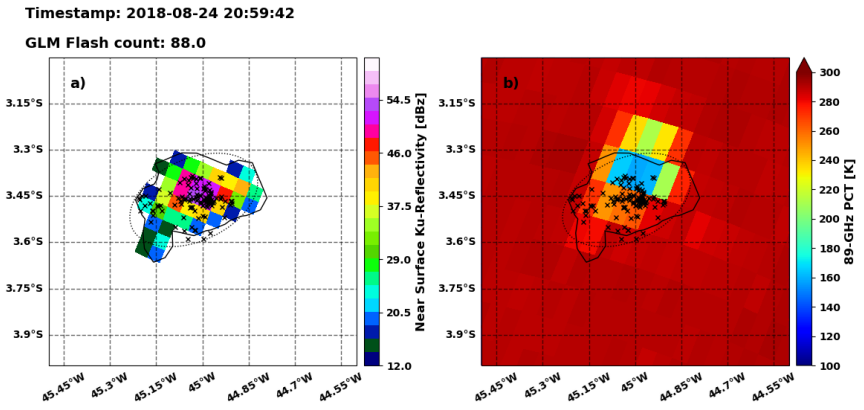

Figure 1. An example showing the collocation between GLM flashes and a GPM rPF on 24 August 2018 at 20:59:42 UTC. Contoured in black is the DPR Ku-derived 0.1 mm hr^{-1} rain rate, the dotted oval denotes the ellipse fit to the rPF, and crosses denote GLM flashes within ± 10 minutes of the rPF overpass time. Color-filled pixels represent a) the *near-surface* Ku-band attenuation-corrected radar reflectivity [dBz] and b) GMI $Tb_{89\text{-PCT}}$ [K].

2.4 Thermodynamic parameters

We extract environmental parameters from the ERA5 (Copernicus Climate Change Service 2017) to examine the thermodynamic and dynamic environments of electrically active cPFs. It has a 0.25° x 0.25° horizontal grid spacing and hourly time steps. The ERA5 data is taken at the grid point nearest to the center and time of each PF, although due to temporal differences as well as ERA5 spatial resolution, grid points selected may not necessarily be representative of the formation environment. The different ERA5 reanalysis variables (file variable names) and their characteristics used in this study are as follows: geopotential (z), temperature (t), relative humidity (r), zonal wind (u), and meridional wind (v).

Numerous previous studies have demonstrated that lightning is strongly correlated with both precipitation ice (e.g., Goodman et al. 1988; Blyth et al. 2001; Petersen et al. 2005; Matthee et al. 2014) and various measures of updraft strength (e.g., Carey and Rutledge 1996; Lang and Rutledge 2002; Deierling and Petersen 2008). Maximum updraft strength can thought of, via kinetic energy considerations, as the square root of twice the CAPE which has also been compared to lightning in several studies (e.g., Price and Rind 1992; Rutledge et al. 1992; Murugavel et al. 2014; Tinmaker et al. 2015; Zheng et al. 2016) with positive correlations being found between lightning and CAPE. More lightning occurs over continental regions where buoyancy profiles favor stronger updrafts than oceanic regions; normalized CAPE (NCAPE) serves as a metric for this vertical distribution of CAPE. Often termed "shape of the CAPE", NCAPE is defined as CAPE divided by the depth of the positively buoyant layer. For the same amount of CAPE, larger (smaller) values of NCAPE indicate a vertically compressed or "fat" (extended or "skinny") buoyancy profile producing larger (more moderate) parcel accelerations (Blanchard 1998). Another advantage of NCAPE over CAPE is that surface elevation is taken into account in this metric, which is important when considering the hemispheric observations of this new database. Previous studies (e.g., Carey and Buffalo 2007; Fuchs et al. 2015) have looked at the correlation between NCAPE and lightning flash rate, but not at the hemispheric scale now afforded by GPM and GLM. We also consider the environment's prognosis of storm mode (e.g., ordinary, supercell, MCS) by computing the Bulk Richardson Number (BRN), which is the ratio between CAPE and the vertical shear through the lowest 6 km (Weisman and Klemp 1982; Thompson et al. 2003); however, it should be noted that this is a complicated number as a low CAPE-low shear environment can give the same BRN as a high CAPE-high shear environment. The most unstable CAPE (MUCAPE),

which is computed using Python's Metpy module (May et al. 2021), is used in the NCAPE and BRN calculations herein.

3 Results

3.1 Geographical Distributions of PFs with GLM lightning

With 3 years of coincident GPM and GLM observations, about 1.2 million rPFs and 1 million cPFs are identified between ±50° latitude and 134°W to 15°W longitude (Table 1). Approximately 2.2% of rPFs and 5.9% of cPFs have at least one flash observed by GLM (hereafter referred to as being "electrically active" [EA]). Roughly 9% and 1% of continental and oceanic rPFs, respectively, are EArPFs. Alternatively, 22% of continental cPFs are EAcPFs, while over the oceans only 2% are EAcPFs. This distinct land/ocean contrast is consistent with previous studies (e.g., Orville & Henderson, 1986; Zipser & Lutz, 1994; Toracinta et al., 2002; Williams & Stanfill, 2002; Christian et al., 2003; Cecil et al., 2005; Liu et al., 2011, 2012). Figure 2 illustrates this land/ocean contrast in EArPFs and EAcPFs, and its extension into the mid and high latitudes. The percent of EArPFs and EAcPFs having only 1 GLM flash does not change between the tropics and midlatitudes for both continental and oceanic PFs (Table 1). However, the overall percentage of EAcPFs increases by roughly 7.5% and 2% for continental and oceanic regions respectively between the tropics and midlatitudes. When EArPFs are considered, the opposite trend is observed; the overall percentage of oceanic EArPFs remains approximately constant while the percentage of continental EArPFs decreases by roughly 4%. This difference is largely due to the lack of stratiform lightning in the winter in the mid-latitudes.

Table 1. Population of rPFs (cPFs) defined by Ku derived rain rate from March 2018 through April 2021 within ±50° N/S and 134°W to 15° W.

	Ocean All lats	Land All lats	Ocean Tropic lats	Land Tropic lats	Ocean Mid lats	Land Mid lats
rPFs (cPFs)	,029,480 (759,416)	,082 (186,119)	,834 (432,345)	,752 (138,727)	,684 (77,428)	,801 (18,611)
EArPFs (EAcPFs)	,118 (15,857)	,158 (40,735)	,823 (7,200)	,857 (26,854)	(2,571)	,608 (5,016)
EArPFs (EAcPFs) with only 1 flash	,664 (4,217)	,691 (6,418)	(1,954)	,509 (4,349)	(775)	(848)

Only 10% of EArPFs and EAcPFs are located outside the TRMM-LIS latitude coverage, which is similar to global lightning patterns observed with the OTD (Christian et al. 2003; Beirle et al. 2014). Although there are more features

observed in tropical latitudes ($|\text{latitude}| \leq \mathbf{20}^{\circ}$) than in the mid-/high latitudes ($|\text{latitude}| \geq \mathbf{35}^{\circ}$), the fraction of EAcPFs within each 1°x1° latitude by longitude grid box to the total number of cPFs within the same grid box increases from ~20-40°N then sharply falls off towards higher latitudes. Meanwhile, in the Southern Hemisphere the fraction of EAcPFs increases from the Equator to ~10-15°S (Figure 2d). These patterns seem tied to the relative proportion of land vs. ocean in each hemisphere. This large drop-off in EAcPFs around 40°N, when compared to cPFs, may also be tied to lower GLM DE at these higher latitudes. Analysis by Cummins (2021) shows that GOES-16 GLM-DE is less than ~70% (55%) during the night (day) at latitudes poleward of 40-45°; one reason for this reduction in GLM-DE at high latitudes is the increase in minimum detectable flash energy at off nadir viewing angles (Marchand et al. 2019; Rutledge et al. 2020). Also, meteorological contributors to this reduced DE may include the prevalence of "anomalously" charged storms (e.g., Fuchs et al. 2015 Figure 2b) in the High Plains region of the United States and Argentina (Orville and Huffines 2001; Zajac and Rutledge 2001; Fuchs et al. 2016, 2018; Medina et al. 2021).

The influence of topography, predominantly over and downstream of orographic regions, on the spatial distribution of EArPFs and EAcPFs over North and South America is evident in Figure 2. For example, in North America, there are fewer EAcPFs over the mountains (west of 100°W), but a larger fraction of those is electrically active compared to the more numerous EAcPFs observed downstream of the mountains (Figure 2d). This is likely associated with terrain serving as an elevated heat source and convective cloud morphologies consisting of shallower warm cloud depths and more dominant ice processes. A somewhat similar pattern is also seen along the Andes. There is also a nonzero percentage of EAcPFs over oceanic features like the Gulf Stream, which is a pattern that has been reported in earlier studies (e.g., Biswas & Hobbs, 1990; Orville, 1990; Virts et al., 2015), as well as the South Atlantic Convergence Zone and the boundary of the Eastern Pacific Intertropical Convergence Zone region off Central America. A relatively larger fraction of cPFs tend to be electrically active towards the mid-latitudes, especially in the Northern Hemisphere (NH), although this may be due to topographic differences and a larger fraction of landmass in the NH. This trend may also be due to synoptic-scale disturbances being more influenced by the westerly jet towards these higher latitudes, where the probability of deep convection (e.g., steeper mid-level lapse rates that promote a more robust rimed ice phase) is enhanced. The enhancement seen over the Andean Plateau (Figure 2d) is likely a result of the South American low level jet transporting moisture to a region of elevated heating (e.g., Insel et al. 2010). Synoptic scale influences are also argued for by the ~8% increase of EAcPFs over the continental mid-latitude regions as compared to tropical regions. Over the oceans, higher ratios are generally adjacent to landmasses.

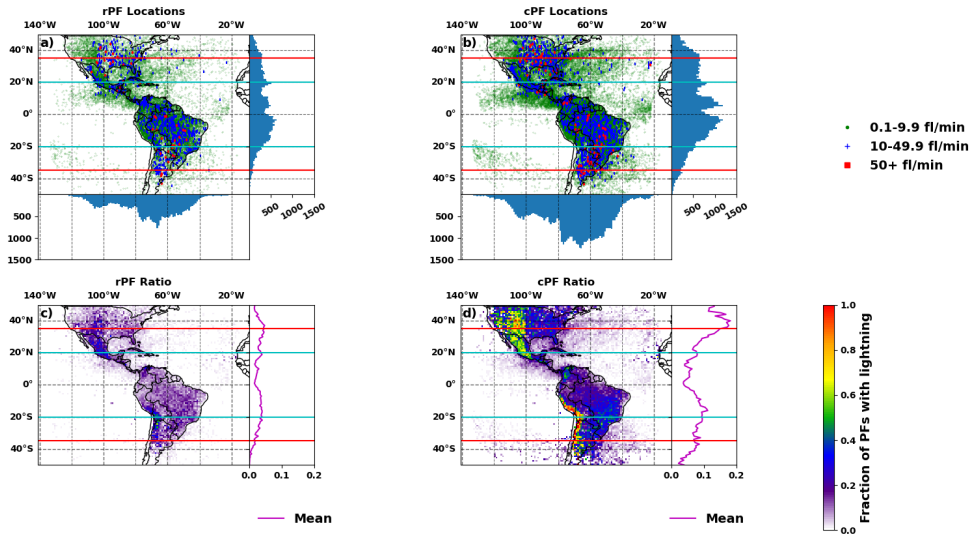

Figure 2. Distribution of EArPFs (panel a) and EAcPFs (panel b) and fraction of EArPFs and EAcPFs relative to the total number of rPFs and cPFs in 1° x 1° boxes (panels c and d, respectively) from March 2018-April 2021 within the GLM FOV. Horizontal lines indicate study regions: the tropics are equatorward of the cyan lines (±20°) and the mid-/high latitudes are poleward of the red lines (± 35°). Latitudinal and longitudinal histograms for EArPFs and EAcPFs in panels a and b as well as the mean (purple) latitudinal distribution of the fraction of electrically active features in panels c and d are also included.

3.2 PF Physical characteristics observed from GPM and GLM

In this and following sections, radar (KuPR) and passive microwave (GMI) characteristics of EArPFs and EAcPFs are discussed. PF radar-derived properties analyzed include maximum height and reflectivity echo area, while GMI-derived properties include minimum PCT at 37- and 89-GHz. These PF characteristics serve as metrics for characterizing the convective state (e.g., Nesbitt et al. 2000; Liu and Zipser 2015). Convective intensity can be inferred from the maximum echo top heights/temperatures of certain thresholds (e.g., 40 dBz/-40°C) as well as minimum PCTs, whereas the radar reflectivity volume or cold brightness temperature area can represent the convective core size and indicate regions of large, rimed ice. As this new lighting-enriched GPM PF database extends to higher latitudes than the TRMM FOV, this study compares the lightning-precipitation patterns in the tropics (e.g., Toracinta et al., 2002; Cecil et al., 2005; Liu et al., 2011, 2012) with those in higher latitudes.

Overall, relationships between GLM flash counts and radar and passive

microwave properties for EAcPFs are similar to those seen in past studies with TRMM (e.g., Nesbitt et al. 2000; Toracinta et al. 2002; Liu et al. 2011, 2012). However, if data for the tropics and mid-/high latitudes are partitioned, a few differences in behavior are observed in the examined variables. Figure 3 presents the relation between GLM flash counts and the temperature of the maximum 30 dBz echo top height (panels a, b; top row) and $PCT_{89\text{-}GHz}$ (panels c, d; bottom row) for the tropics and mid-/high latitudes. As noted in Sec. 2.2, the temperature of the maximum 30 dBz contour is being used as the vertical coordinate (x-axis, Figure 3a, b) because the processes of interest are temperature sensitive, and the temperature structure changes with latitude. There is a clear shift to colder temperatures of the maximum 30 dBz echo top height in the mid-/high latitudes relative to the tropics at lower flash counts (red and brown lines in Figure 3a, 3b); additionally, the median (mean) temperature in the tropics is -20°C (-26°C) with the mid-/high latitudes being 6°C (3°C) colder. A less pronounced shift towards colder microwave Tbs is also observed at higher latitudes in both the $PCT_{89\text{-}GHz}$ (Figure 3d) and $PCT_{37\text{-}GHz}$ (not shown) for EAcPFs with 1 GLM flash; median and mean values for EAcPFs in the mid-/high latitudes are 6°C and 5°C warmer respectively when compared to EAcPFs in the tropics. It should be noted that a systematic shift towards colder brightness temperatures at higher latitudes (Figures 3c, 3d) similar to that in temperature of the maximum 30 dBz echo (Figures 3a, 3b) is not observed. The colder 30 dBz echo tops in the mid-/high latitudes may indicate stronger updrafts than in the tropics. It should be noted that PCT is a measure of the columnar ice amount and hence more indirectly related to updraft intensity, whereas radar echo top is a direct measure of lofting of mass.

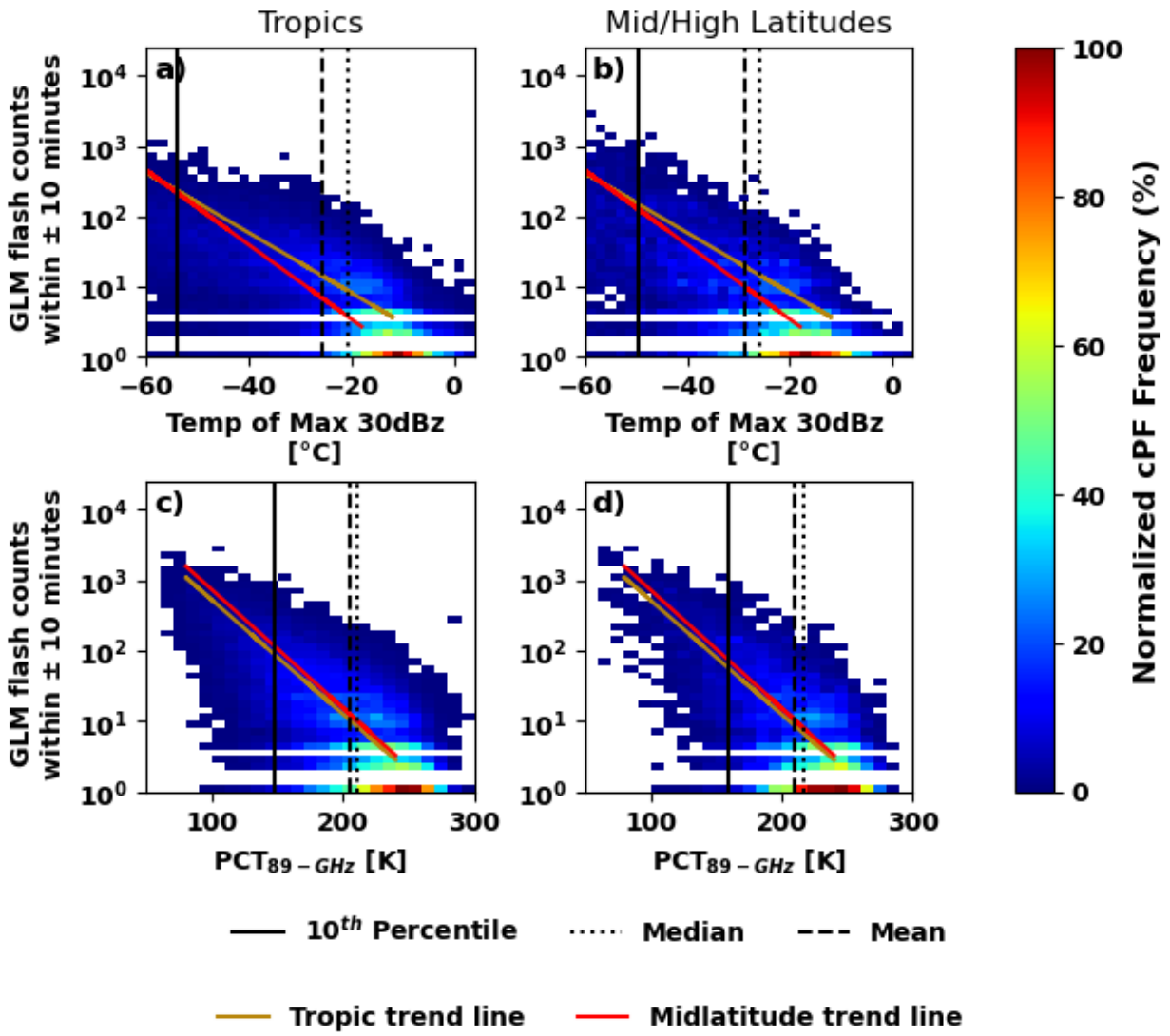

Figure 3. cPF GLM flash counts related to the temperature [°C] of maximum 30 dBz echo top height (panels a, b; top row) and $PCT_{89\text{-}GHz}$ [K] (panels c, d; bottom row) for the tropics (panels a, c; left column) and the mid-/high latitudes (panels b, d; right column). The 10^{th} percentile (solid), median (dotted), and mean values (dashed) are also shown for each panel. A best-fit temperature mode trend line for the tropics (brown) and midlatitudes (red) are shown for the GLM flash counts vs. temperature of the maximum 30 dBz echo top height (panels a, b; mode values not shown).

3.3 PF convective properties in the context of lightning flash rate tendencies

3.3.1 Radar

To examine the temporal behavior of GPM's PF sampling at various stages in the convective life cycle, we analyze the mean GLM flash rate change for EArPFs and EAcPFs over ±10-minute interval centered on the GPM-CO overpasses in terms of feature area and its 30-dBz echo top height (Figure 4). The mean flash rate change (e.g., Figure 4a, c) is used as a proxy for monitoring the feature evolution relative to the GPM overpass. Since the mean flash rate change can be influenced by a few PFs, the percent of PFs with increasing flash rates (e.g, Figure 4b, d) is also examined. Increasing mean flash rates during a 20-minute window should, though not always, indicate features that are intensifying (e.g., an EAcPF with no flashes observed before the overpass time and 10 flashes after the overpass time would result in a flash rate change of 0.5 fl min^{-1}). It should be noted that in Figure 4b, d that EArPFs/EAcPFs with decreasing or no change flash rate can be inferred from the converse percentage of features with increasing flash rates (e.g., if 20% of EAcPFs have increasing flash rates then 80% have either decreasing or no change in flash rate).

Maturing convection tends to have increasing flash rates and smaller PF areas, whereas decaying MCS-like systems have larger PF areas and decreasing flash rates (Toracinta et al. 2002; Liu et al. 2008; Makowski et al. 2013). EAPFs characterized by 30-dBz echo top heights between 6 and 10 km with areas 1000 km^2, and a positive mean flash rate change are hypothesized to be maturing convection (Figure 4a, c). At least 65% of EArPFs and between 50-60% of EAcPFs are inferred to be maturing convection utilizing these criteria. These features are associated with more GLM flashes after the overpass time, which could be result of strengthening updrafts (hence the increase in 30-dBz echo top heights). The tropics (equatorward of ± 20°) contain 62% of EArPFs and 61% of EAcPFs meeting the aforementioned criteria (not shown). EAPFs characterized by the highest observed 30-dBz echo top heights (~18 km) and increasing flash rates tend to have areas spanning from 1,000-10,000 km^2 and may be indicative of intense deep convection in growing MCSs.

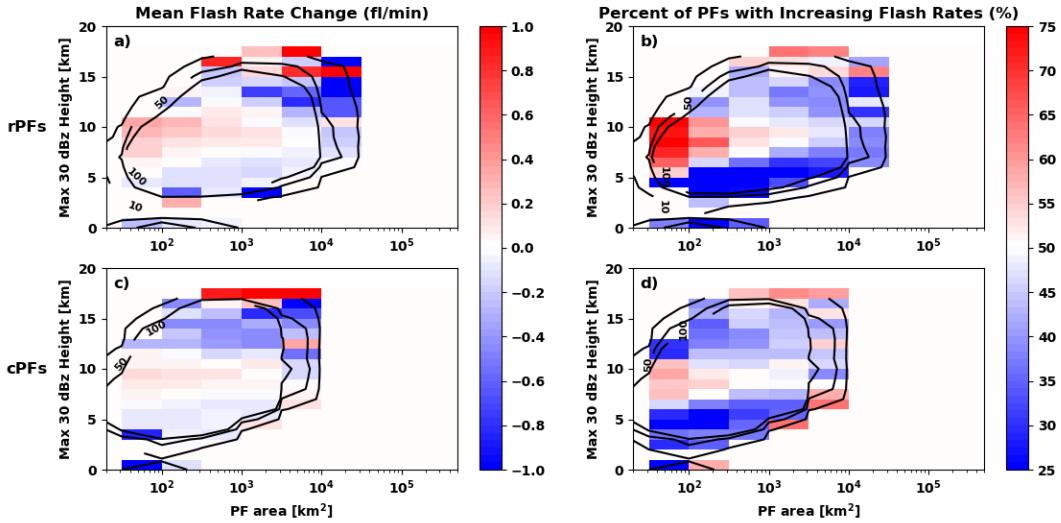

Figure 4. Bi-variate distribution of mean flash rate change (fl min^{-1}; panels a and c; left column) and fraction of PFs with increasing flash rates (%; panels b and d; right column) as a function of 30-dBz echo top height (km) and PF area (km^2) from all samples containing at least one flash. EArPFs are plotted in panels a and b; EAcPFs are plotted in panels c and d. Black contours indicate the number of samples in each bin.

The mean flash rate for both EArPFs and EAcPFs is examined in terms of the IWM between -5°C and -35°C (Eq. 1) where reflectivity exceeds 30 dBz versus the percentage of the 20 dBz echo volume containing 30 dBz in that same temperature region (Figure 5). The percentage of the 20 dBz echo volume above the freezing level containing at least 30 dBz can be used as a proxy for identifying graupel as the higher reflectivity values are correlated to larger ice particles. Higher percentages would indicate a larger graupel fraction is contained within the volume, consistent with earlier stages of the convective life cycle (e.g., Carey and Rutledge 1996; Bringi et al. 1997). Consistent with the radar-derived trends noted in Figure 4, there is a marked increase in the fraction of EAPFs with increasing flash rates when the ice regions are dominated by reflectivity values greater than 30 dBz (Figure 5b, d). For example, in Figure 5d, for an ice mass of 1 x 10^8 kg, if the volume fraction of reflectivity 30 dBz exceeds 40% within the mixed phase region, the EAcPF will most likely have an increasing flash rate. Additionally, if an EArPF has a volume fraction of reflectivity 30 dBz exceeds 40% within the mixed phase region, it will typically have an increasing mean flash rate regardless of the IWM within the same region (Figure 5a). Although these trends are similar regardless of whether the EAPF occurs in the tropics or mid-/high latitudes, there is less distinction between mid-/high latitude EAPFs with increasing flash rates and those with steady or

decreasing flash rates (not shown).

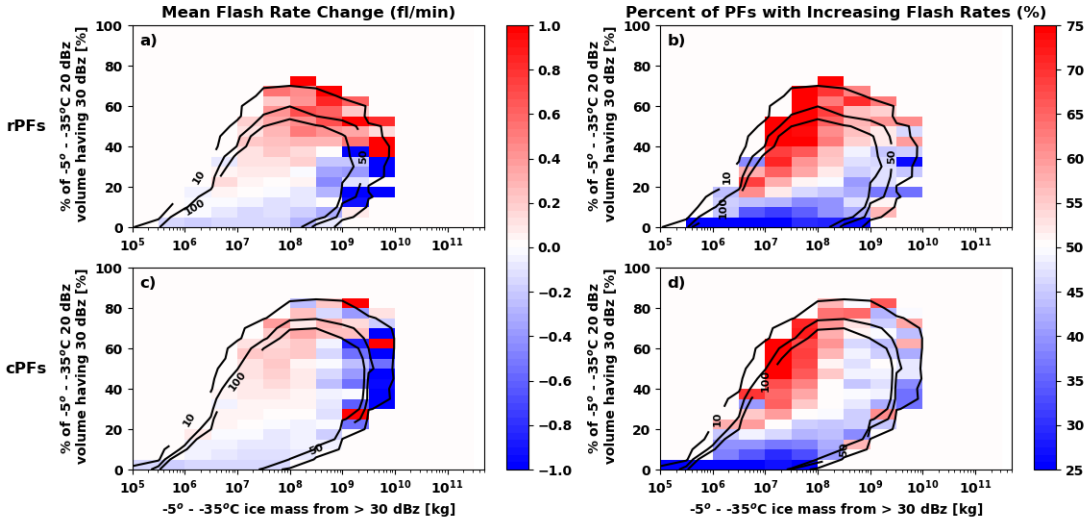

Figure 5. As in Figure 4, except as a function of ice mass between -5°C and -35°C in excess of 30 dBz and the percent of the 5°C and -35°C 20 dBz volume having 30 dBz.

3.3.2 Passive Microwave

The two main GMI channels utilized in this study are 89-GHz and 37-GHz, which are sensitive to large ice scattering and highly correlated to lightning flash rates (Driscoll 1999, Blyth et al. 2001; Cecil et al. 2005; Liu et al. 2011). In terms of feature area and PCT_{89GHz}, there are slight differences in the flash rate change of EArPFs and EAcPFs (Figure 6). Features with $PCT_{89GHz} < 150$ K tend to have decreasing flash rates at the GPM overpass time, regardless of the EAPF area (Figure 6a, c). We hypothesize these features are associated with decaying organized convection (e.g., MCSs) that still contain considerable ice water aloft but lack sufficient vertical motions to sustain electrical charging rates. Intensifying EArPFs are characterized by increasing flash rates and feature areas < 100 km^2, while PCTs are relatively warm at 89- (above 250 K; Figure 6a,b) and 37-GHz (not shown). These general trends persist regardless of bin size. Additionally, these relatively warm EArPFs have no (or very few) flashes detected before the GPM overpass with increased flash activity after it, suggesting that these features may be in the early stages of the convective life cycle when the updraft is intensifying but a robust ice phase has yet to develop to the point that it significantly reduces the upwelling microwave radiation. The $PCT_{89\text{-}GHz}$ associated with these features might continue to decrease from an increasing amount of ice scattering resulting in lightning discharges that happen after the GPM overpass time, but still within the 20-minute convective

window. Furthermore, these warmer brightness temperatures might also be due to surface contamination in non-uniform beam filling in smaller PFs (i.e., profiles along PF edges may contain less ice than profiles in the center of a PF). For a given EAcPF area, a threshold $PCT_{89\text{-}GHz}$ is needed to be reached before EAcPFs transition from non-increasing to increasing flash rates (Figure 6d). This threshold PCT can be calculated using Equation (2):

$$\mathbf{PCT = 337.2 - 40.9 \cdot \log_{10}(\text{Area})} \quad (2)$$

where the resulting Tb is in K, and the EAcPF area is in km^2.

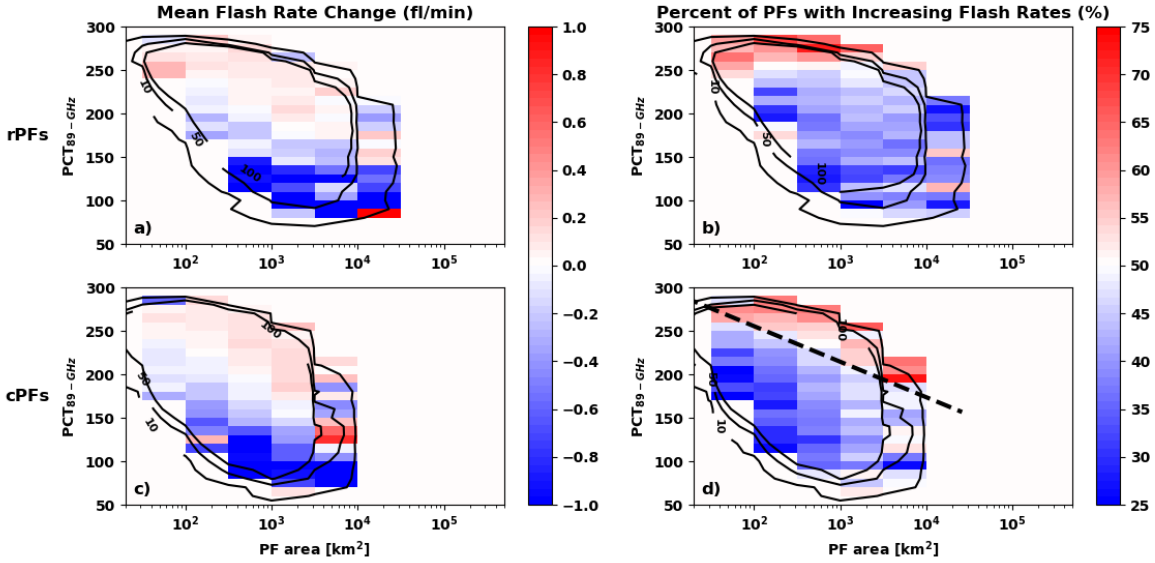

Figure 6. As in Figure 4, except as a function of feature area and minimum 89-GHz PCT. The black dashed line in panel d) represents Equation 2.

3.4 Environmental properties

We use the GLM-enriched GPM PF database to examine how trends in storm precipitation and lightning properties vary as a function of large-scale environment across the increased spatial domain of the GOES-East FOV. Although flash rate tends to be more commonly used in literature and is much more intuitive than flash density, flash density is used in this section to qualify PF "intensity". Because flash density normalizes flash rate by PF area, it should be noted that flash densities can be somewhat ambiguous since different flash densities can produce similar flash rates depending on the PF area. EAcPFs with relatively low (lowest 10% with at least one lightning flash; 2.55×10^{-3} fl km^{-2}

(20 min)$^{-1}$) and relatively high (highest 90%; 1.04x10^{-1} fl km^{-2} (20 min)$^{-1}$) flash activity are examined in terms of GPM properties and environment. EAcPFs with high flash densities have $PCT_{89\text{-}GHz}$ ($PCT_{37\text{-}GHz}$) that are 39 K (24 K) colder than their low-density counterparts. They also have areas of the 30 dBz echo at 7 km, which is located well within the mixed phase region, that are at least 250 km^2 larger than those with low flash densities (not shown). This is consistent with the conceptual model of stronger and wider areas of updraft producing more ice condensate in the charging zone and thus enhancing the lightning activity.

Figure 7 and Table 2 demonstrate how the GLM flash density and GPM properties for the EAcPFs relate to their environment. For example, in Figure 7, each row of panels represents a different GPM property examined (e.g., $PCT_{89\text{-}GHz}$), with each column of panels representing a different environmental property. Both NCAPE and BRN are prognostic metrics, representing the pre-convective state of the environment, while the GPM derived IWM (Eq. 1) represents a diagnostic metric that depicts the result of the environmental forcing. Additionally, EAcPFs are removed if values of NCAPE or BRN from environmental analysis were physically unrealistic (e.g., NCAPE < 0, BRN < 0, or BRN > 400; Thompson et al. 2003). Colors within each panel represent different quartiles of the environmental variable (Table 2).

Table 2. Environmental quartile values for Figures 7 and 8.

	Q1 (25th percentile)	Q2 (25th – 50th percentile)	Q3 (50th percentile – 75th percentile)
IWM [kg]	$< 2.48 \times 10^4$	2.48x10^4–7.32x10^4	7.32x10^4–2.02x10^5
NCAPE [m s^{-2}]	$< 5.25 \times 10^{-2}$	5.25x10^{-2}–9.82x10^{-2}	9.82x10^{-2}–1.63x10^{-1}
BRN []	$< 1.73 \times 10^1$	1.73×10^1–7.76x10^1	7.76x10^1–1.84x10^2

Figure 7 suggests that as observed IWM increases, $PCT_{89\text{-}GHz}$, $PCT_{37\text{-}Ghz}$, and the temperature of the 30 dBz echo top height all decrease for both high and low flash density EAcPFs (Figure 7a, 7d, 7g), although there does tend to be a larger spread for high flash density EAcPFs. This is not unexpected as an increased amount of precipitable ice will produce a Tb depression at microwave frequencies sensitive to ice scattering (Spencer et al. 1989). Figure 7 shows that there is an approximately 40 K (24 K) difference for the mean $PCT_{89\text{-}GHz}$ ($PCT_{37\text{-}GHz}$) between the low and high flash density EAcPFs. Additionally, there is almost a 28°C difference in the temperature of the 30 dBz echo top height. These mean differences can be inferred for all environmental and GPM variables, although it is more easily seen in NCAPE/BRN and $PCT_{37\text{-}GHz}$/temperature of the maximum 30 dBz echo top height (Figure 7e, 7f, 7h, 7i). Moreover, it should be noted that high flash density EAcPFs also tend to have a larger spread in all GPM properties regardless of environmental variable. Figure 7 also shows that low flash density EAcPFs have increased Tbs correlated to higher NCAPE values (Figure 7b, 7e); further analysis shows that this relationship seems to be

driven by oceanic EAcPFs, especially those in the tropics (not shown).

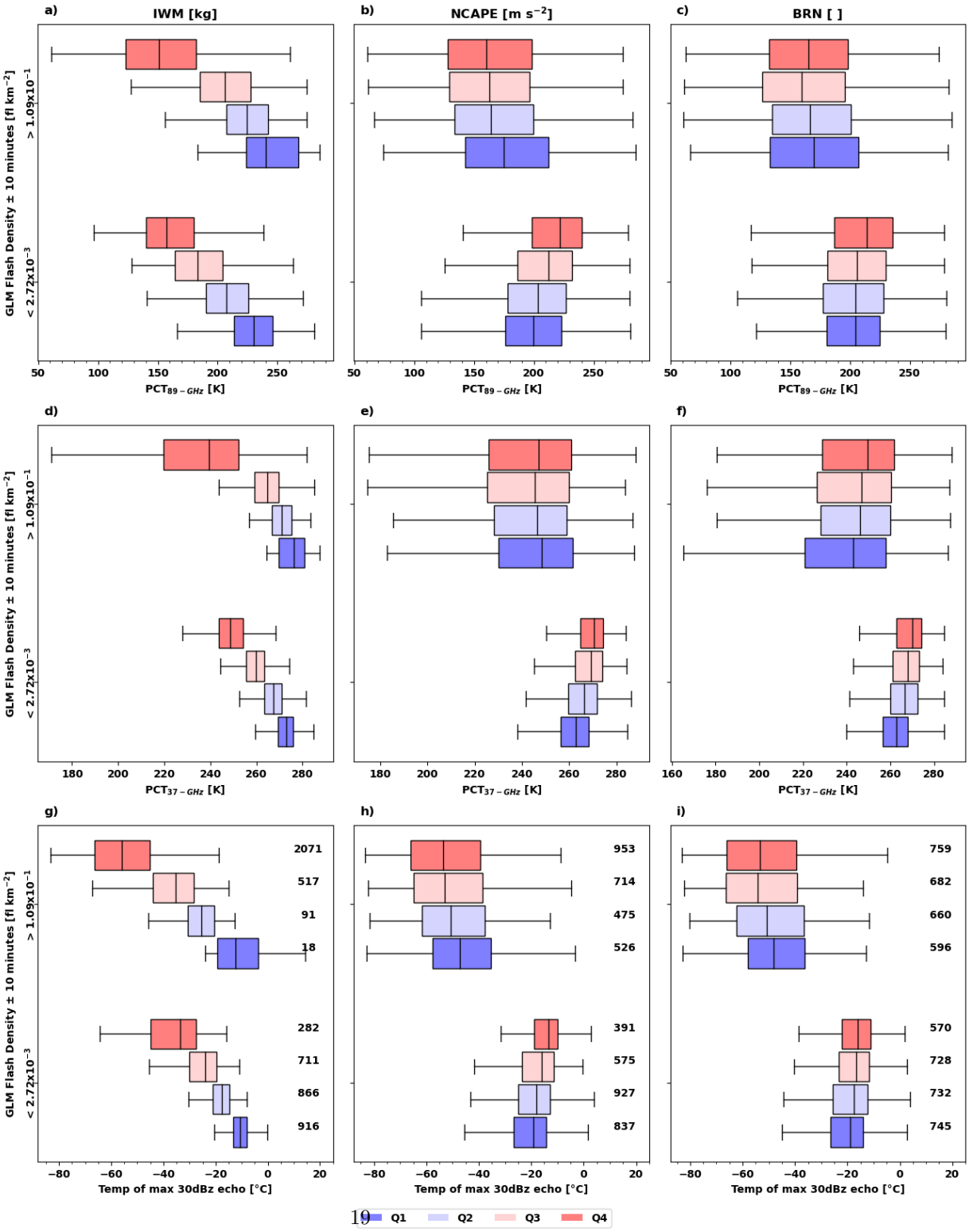
a)
IWM [kg]
b)
NCAPE [m s^{-2}]
c)
BRN [ ]
d)
e)
f)
g)
h)
i)
GLM Flash Density ± 10 minutes [fl km^{-2}]
> 1.09x10^{-1}
< 2.72x10^{-3}
PCT$_{89-GHz}$ [K]
PCT$_{37-GHz}$ [K]
Temp of max 30dBz echo [°C]
2071
517
91
18
282
711
866
916
953
714
475
526
391
575
927
837
759
682
660
596
570
728
732
745
Q1
Q2
Q3
Q4

Figure 7. Box and whisker plots examining how GLM flash density (lowest 10 and highest 90 percentiles, y-axis) relates to GPM radar and passive microwave properties for EAcPFs as a function of environment (shaded by quartile, see Table 2 for values for Q1-Q4) for a-c) PCT89GHz [K], d-f) PCT37GHz [K], and g-i) temperature of the maximum 30 dBz echo top height [°C], x-axis. Boxplots extend from the first to third quartiles of the data, with a line at the median and whiskers extend from the box by 1.5x the inter-quartile range. Outliers are not plotted. Sample sizes are shown in panels g-i) but valid for other panels within the same column.

Figure 8 examines the relative geographical distributions of the ratio of EAcPFs in the fourth quartile of NCAPE, BRN, and IWM (Table 2; Figures 8b, 8c, and 8d respectively) to the total count of EAcPFs (Figure 8a) in 2° x 2° latitude by longitude boxes. Although not shown, most EAcPFs within the fourth quartile of NCAPE are continental, which gives us confidence in the relative distribution of the model-derived NCAPE utilized. High percentages of EAcPFs characterized by high values of NCAPE (i.e., stronger updrafts) approximately encompass or "ring" the transition to increased elevations surrounding the Amazon River Basin along with the Lake Maracaibo region in Venezuela (Figure 8b). In comparison, the La Plata River Basin in Argentina/Brazil as well as the Great Plains region in the United States both tend to have a more pronounced percentage of EAcPFs characterized by higher GPM-estimated IWM (Figure 8d), although the pattern over the US is not as distinct. This behavior is in stark contrast to the rather unremarkable behavior in IWM over and along the fringes of the Amazon, where marked signatures in both NCAPE and BRN are observed. The two aforementioned regions of enhanced IWM behavior for EAcPFs do seem to correspond to mid-latitude regions where hailstorms and often inverted polarity lightning storms are observed, which may be why we see a larger fraction of *GLM*-based EAcPFs in Argentina than the Northern Great Plains (Lang et al. 2020; Rutledge et al. 2020; Medina et al. 2021). The La Plata river basin also seems to be an area of slightly enhanced flash densities (not shown). Areas of larger EAcPF BRN tend to occur in the tropics (Figure 8c), perhaps pointing to more frequent occurrence of less organized, more upright EA convection in the tropics. Analysis of the lowest quartile of these three variables shows very noisy distributions with higher percentages typically observed over oceanic regions (not shown). Spatial distributions for the percentage of EAcPFs within the upper quartile of all three variables (i.e., EAcPFs with large NCAPE *and* IWM *and* BRN) are analyzed; there are no distinct spatial patterns where high relative percentages of these EAcPFs occur (not shown). It should be noted though, that spatial distributions such as the ones discussed in this section may be a reflection of the low sample numbers of EAcPFs in some regions of Figure 8a. Results show that higher flash densities tend to occur with higher values of IWM and NCAPE as expected (not shown) and that isolating lightning forcing mechanisms when looking at estimated ice mass or NCAPE (a proxy for vertical updraft speed) on a hemispheric or larger regional scale may be possible, although more research and samples are needed in this area.

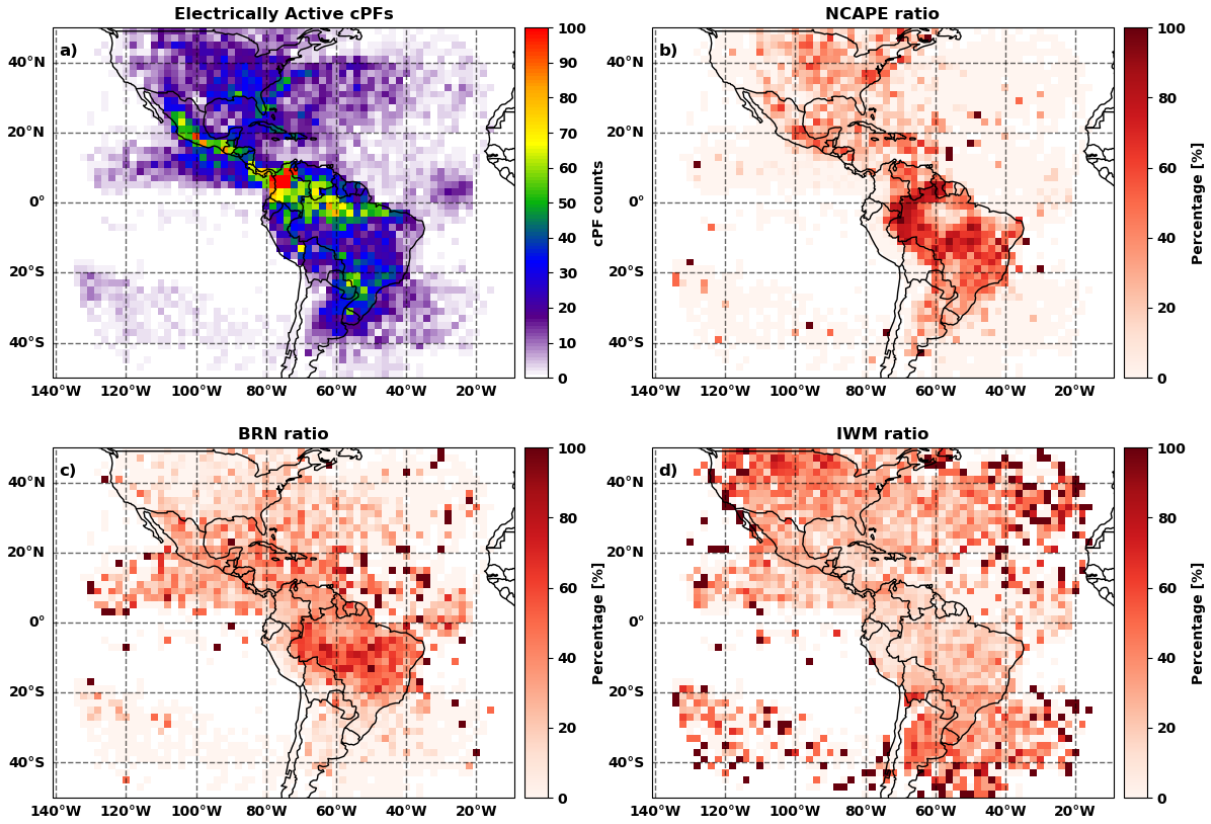

Figure 8. Distribution of the percentage of EAcPFs above the 75th percentile of NCAPE (panel b), BRN (panel c), and IWM (panel d) to the count of EAcPFs (panel a) in 2° x 2° boxes.

4 Summary and Conclusions

GLM and GPM observations supplement and extend studies of space-based total (in cloud and cloud-to-ground components) lightning and precipitation observations (e.g., TRMM) into the mid-/high latitudes, where such coincident observations were previously unavailable over many regions of the globe. The lightning-enriched GPM precipitation feature (PF) database compiled and analyzed for this study illustrates how snapshots of convective cloud precipitation profiles and radiative metrics observed from low-Earth orbiting satellites (e.g., GPM) can be combined with lightning observations collected in a more temporally continuous fashion from geostationary satellites (e.g., GLM). Using 3 years of coincident GLM and GPM observations, relationships between lightning flash rates and radar (Ku-band) and passive microwave properties of precipitation features (PFs) in the tropics and mid-/high latitudes are investigated. The main findings of this study are as follows:

1) GLM data analyzed in the context of GPM PFs provides results consistent with and extends earlier studies that are centered on the tropics. The maximum height of the 30 dBz echo of electrically active convective PFs (EAcPFs) reaches 6°C colder temperatures on average in the mid-/high latitudes than in the tropics. For all flash counts observed, there is a systematic shift towards colder temperatures at higher latitudes (Figure 3).

2) There is a clear delineation between cPFs with increasing electrical activity vs. those with decreasing or no change in electrical activity. EAcPFs with increasing flash rates tend to be smaller in size with relatively warmer PCTs at 89-GHz. These are likely at the early/growth stage of the convective life cycle, whereas decaying MCS-like features exhibit larger PF areas, colder Tbs, and decreasing flash rates (Figure 6). As these cPFs grow in horizontal size, colder Tbs seem to be needed for them to continue producing more flashes.

3) EAcPFs with both low and high flash densities are associated with different IWM and are characterized by corresponding trends in radar and passive microwave observations; for other environmental influences, the relative influence/role on the convective intensity of EAcPFs is not as clear (Figure 7). Geographically, the La Plata River basin in Argentina and Great Plains region in the United States, which were previously under-sampled by coincident lightning and precipitation measurements, are characterized by large percentages of EAcPFs with relatively stronger convective potential (as estimated by NCAPE) and larger values of GPM-estimated IWM. In particular, there is a large fraction of EAcPFs with enhanced NCAPE that appear to be anchored to enhanced topography encircling the Amazon basin (Figure 8b).

Acknowledgments

This work was supported by NASA MSFC Award NNM11AA01A and by Dr. Gail Skofronick-Jackson through NASA's Internal Scientist Funding Model in the Weather and Atmospheric Dynamics Program at NASA Headquarters. Coauthor Liu acknowledges support from NASA MSFC Grant NNX17AI99G. The views, opinions, and findings in this report are those of the authors and should not be construed as an official NASA or U.S. government position, policy, or decision.

Open Research

All GPM precipitation feature data is available at http://atmos.tamucc.edu/trmm/data/gpm/. The GLM data are available via the National Oceanic and Atmospheric Administration (NOAA) Comprehensive Large Array-data Stewardship System (CLASS).

References

Bateman, M., & Mach, D. (2020). Preliminary detection efficiency and false alarm rate assessment of the Geostationary Lightning Mapper on

the GOES-16 satellite. *Journal of Applied Remote Sensing*, **14**, 1, https://doi.org/10.1117/1.jrs.14.032406.Beirle, S., Koshak, W., Blakeslee, R., & Wagner, T. (2014). Global patterns of lightning properties derived by OTD and LIS. *Natural Hazards Earth System Science*, **14**, 2715–2726, https://doi.org/10.5194/nhess-14-2715-2014.Biasutti, M., Yuter, S. E., Burleyson, C. D., & Sobel, A. H. (2012). Very high resolution rainfall patterns measured by TRMM precipitation radar: Seasonal and diurnal cycles. *Climate Dynamics*, **39**, 239–258, https://doi.org/10.1007/s00382-011-1146-6.Biswas, K. R., & Hobbs, P. V. (1990). Lightning over the Gulf Stream. *Geophysical Research Letters*, **17**, 941–943, https://doi.org/10.1029/GL017i007p00941.Blanchard, D. O. (1998). Assessing the vertical distribution of convective available potential energy. *Weather and Forecasting*, **13**, 870–877, https://doi.org/10.1175/1520-0434(1998)013<0870:atvdoc>2.0.co;2.Blyth, A. M., Christian,H. J., Driscoll,K., Gadian, A. M. & Latham, J. (2001). Determination of ice precipitation rates and thunderstorm anvil ice contents from satellite observations of lightning. *Atmospheric Research*, **59–60**, 217–229, https://doi.org/10.1016/S0169-8095(01)00117-X.Boccippio, D. J., Goodman, S. J. & Heckman, S. (2000). Regional differences in tropical lightning distributions. *Journal of Applied Meteorology*, **39**, 2231–2248, https://doi.org/10.1175/1520-0450(2001)040<2231:RDITLD>2.0.CO;2.Boccippio, D. J., Petersen,W. A., & Cecil, D. J. (2005). The tropical convective spectrum. Part I: Archetypal vertical structures. *Journal of Climate*, **18**, 2744–2769, https://doi.org/10.1175/JCLI3335.1.Bringi, V. N., Knupp, K., Detwiler,A., Liu, L., Caylor, I. J., & Black, R. A. (1997). Evolution of a Florida thunderstorm during the convection and precipitation/electrification experiment: The case of 9 August 1991. *Monthly Weather Review*, **125**, 2131–2160, https://doi.org/10.1175/1520-0493(1997)125<2131:EOAFTD>2.0.CO;2.Carey, L. D., & Buffalo, K. M. (2007). Environmental control of cloud-to-ground lightning polarity in severe storms. *Monthly Weather Review*, **135**, 1327–1353, https://doi.org/10.1175/MWR3361.1.Carey, L. D., & Rutledge, S. A. (1996). A multiparameter radar case study of the microphysical and kinematic evolution of a lightning producing storm. *Meteorology and Atmospheric Physics*, **59**, 33–64, https://doi.org/10.1007/BF01032000.Carey, L. D., & Rutledge, S. A. (2000). The relationship between precipitation and lightning in tropical island convection: A C-Band polarimetric radar study. *Monthly Weather Review*, **128**, 2687–2710, https://doi.org/10.1175/1520-0493(2000)128<2687:TRBPAL>2.0.CO;2.Carey, L. D., Schultz, E. V., Schultz, C. J., Deierling, W., Petersen, W. A., Bain, A. L., & Pickering, K. E. (2019). An evaluation of relationships between radar-inferred kinematic and microphysical parameters and lightning flash rates in Alabama storms. *Atmosphere*, **10**, 1–36, https://doi.org/10.3390/atmos10120796.Carlomusto, M. (2019). *GOES-R Series Product Definition and Users' Guide*. 387 pp. Available at https://www.goes-r.gov/products/docs/PUG-L2+-vol5.pdf%0Ahttps://www.goes-r.gov/users/docs/PUG-main-vol1.pdf.Cecil, D. J., & Chronis, T. (2018). Polarization-corrected temperatures for 10-, 19-, 37-, and 89-GHz passive microwave frequencies. *Journal of Applied Meteorology and Clima-*

tology, **57**, 2249–2265, https://doi.org/10.1175/JAMC-D-18-0022.1.Cecil, D. J., & Zipser, E. J. (2002). Reflectivity, ice scattering, and lightning characteristics of hurricane eyewalls and rainbands. Part II: Intercomparison of observations. *Monthly Weather Review*, **130**, 785–801, https://doi.org/10.1175/1520-0493(2002)130<0785:RISALC>2.0.CO;2.Cecil, D. J., Zipser, E. J., & Nesbitt, S. W. (2002). Reflectivity, ice scattering, and lightning characteristics of hurricane eyewalls and rainbands. Part I: Quantitative description. *Monthly Weather Review*, **130**, 769–784, https://doi.org/10.1175/1520-0493(2002)130<0769:RISALC>2.0.CO;2.Cecil, D. J., Goodman, S. J., Boccippio, D. J., Zipser, E. J., & Nesbitt, S. W. (2005). Three years of TRMM precipitation features. Part I: Radar, radiometric, and lightning characteristics. *Monthly Weather Review*, **133**, 543–566, https://doi.org/10.1175/MWR-2876.1.Christian, H. J., Blakeslee, R. J., Goodman, S. J., Mach,D. A., Stewart,M. F., Buechler,D. E., et al. (1999): The Lightning Imaging Sensor. *NASA Conf. Publ.*, 1-4. Available at https://ntrs.nasa.gov/citations/19990108789.Christian, H. J., Blakeslee, R. J., Boccippio, D. J., Boeck, W. L., Buechler, D. E., Driscoll, K. T., et al. (2003). Global frequency and distribution of lightning as observed from space by the Optical Transient Detector. *Journal of Geophysical Research*, **108**, 1–15, https://doi.org/10.1029/2002JD002347.Copernicus Climate Change Service (2017). ERA5: Fifth generation of ECMWF atmospheric reanalyses of the global climate. *Copernicus Climate Change Service Climate Data Store*,. https://cds.climate.copernicus.eu/#!/search?text=ERA5&type=dataset. [Dataset.] (Accessed October 13, 2021).Cummins, K. L. (2021). On the spatial and temporal variation of GLM flash detection and how to manage it. *10th Conference on the Meteorological Application of Lightning Data*, Virtual, 692 https://ams.confex.com/ams/101ANNUAL/meetingapp.cgi/Paper/382589.Deierling, W., & Petersen, W. A. (2008). Total lightning activity as an indicator of updraft characteristics. *Journal of Geophysical Research*, **113**, 1–11, https://doi.org/10.1029/2007JD009598.Driscoll, K. T. (1999). A comparison between lightning activity and passive microwave measurements. *Proceedings 11th International Conference on Atmospheric Electricity*, Guntersville, AL, International Commission on Atmospheric Electricity, 523–526.Fuchs, B. R., Bruning, E. C., Rutledge, S. A., Carey, L. D., Krehbiel, P. R.. & Rison, W. (2016). Climatological analyses of LMA data with an open-source lightning flash-clustering algorithm. *JGR Atmos.*, **120**, 8625–8648, https://doi.org/10.1002/2015JD024663.Fuchs, B. R., Rutledge,S. A., Bruning, E. C., Pierce,J. R., Kodros,J. K., Lang, T. J. et al. (2015). Environmental controls on storm intensity and charge structure in multiple regions of the continental United States. *Journal of Geophysical Research*, **120**, 6575–6596, https://doi.org/10.1002/2015JD023271.Fuchs, B. R., Rutledge, S. A., Dolan, B., Carey, L. D., & Schultz, C. (2018). Microphysical and kinematic processes associated with Anomalous charge structures in isolated convection. *Journal of Geophysical Resesearch: Atmospheres*, **123**, 6505–6528, https://doi.org/10.1029/2017JD027540.Gatlin, P. N., & Goodman, S. J. (2010). A total lightning trending algorithm to identify severe

thunderstorms. *Journal of Atmospheric and Oceanic Technology*, **27**, 3–22, https://doi.org/10.1175/2009JTECHA1286.1.Goodman, S. J., Buechler, D. E., Wright, P. D., & David, W. (1988). Lightning and precipitation history of a microburst-producing storm. *Geophysical Research Letters*, **15**, 1185–1188, https://doi.org/10.1029/GL015i011p01185.Goodman, S. J., Blakeslee, R. J., Koshak, W. J., Mach, D., Bailey, J., Buechler, D., et al. (2013). The GOES-R Geostationary Lightning Mapper (GLM). *Atmospheric Research*, **125**–**126**, 34–49, https://doi.org/10.1016/j.atmosres.2013.01.006.Hersbach, H., Bell, B., Berrisford, P., Hirahara, S., Horanyi, A., Munoz-Sabater, J., et al. (2020). The ERA5 global reanalysis. *Quarterly Journal of the Royal Meteorological Society*, **146**, 1999–2049, https://doi.org/10.1002/qj.3803.Hou, A. Y., Kakar, R. K., Neeck, S., Azarbarzin, A. A., Kummerow, C. D., Kojima, M., et al. (2014). The Global Precipitation Measurement Mission. *Bulletin of the American Meteorological Society*, 701–722, https://doi.org/10.1175/BAMS-D-13-00164.1.Houze Jr., R. A., Rasmussen, K. L., Zuluaga, M. D., & Brodzik, S. R. (2015). The variable nature of convection in the tropics and subtropics: A legacy of 16 years of the Tropical Rainfall Measuring Mission satellite. *Reviews of Geophysics*, **53**, 1–28, https://doi.org/10.1002/2015RG000488.Huffman, G. J., Adler, R. F., Bolvin, D. T., Gu, G., Nelkin, E. J., Bowman, K. P., et al. (2007). The TRMM Multisatellite Precipitation Analysis (TMPA): Quasi-global, multiyear, combined-sensor precipitation estimates at fine scales. *Journal of Hydrometeorology*, **8**, 38–55, https://doi.org/10.1175/JHM560.1.Iguchi, T., Seto, S., Meneghini, R., Chandrasekar, V., & Kubota, T. (2017). *GPM/DPR Level-2 algorithm theoretical basis document*. 1-81 pp. https://www.eorc.jaxa.jp/GPM/doc/algorithm/ATBD_DPR_201708_whole_1.pdf.In
N., Poulsen, C. J., & Ehlers, T. A. (2010). Influence of the Andes Mountains on South American moisture transport, convection, and precipitation. *Climate Dynamics*, **35**, 1477–1492, https://doi.org/10.1007/s00382-009-0637-1.Kummerow, C. D., Barnes, W., Kozu, T., Shiue, J., & Simpson, J. (1998). The Tropical Rainfall Measuring Mission (TRMM) sensor package. *Journal of Atmospheric and Ocean Technology*, **15**, 809–817, https://doi.org/10.1175/1520-0426(1998)015<0809:TTRMMT>2.0.CO;2.Lang, T. J., & Rutledge, S. A. (2002). Relationships between convective storm kinematics, precipitation, and lightning. *Monthly Weather Review*, **130**, 2492–2506, https://doi.org/10.1175/1520-0493(2002)130<2492:RBCSKP>2.0.CO;2.Lang,
T. J., Avila, E. E., Blakeslee, R. J., Burchfield, J., Wingo, M., Bitzer, P. M,. et al. (2020). The RELAMPAGO lightning mapping array: Overview and initial comparison with the Geostationary Lightning Mapper. *Journal of Atmospheric and Oceanic Technology*, **37**, 1457–1475, https://doi.org/10.1175/JTECH-D-20-0005.1.Lau, N.-C., & Crane, M. W. (1995). A satellite view of the synoptic-scale organization of cloud properties in midlatitude and tropical circulation systems. *Monthly Weather Review*, **123**, 1984–2006, https://doi.org/10.1175/1520-0493(1995)123<1984:ASVOTS>2.0.CO;2.Liu,
C. (2016): *GPM precipitation feature database*. 1-15 pp. Available at http://atmos.tamucc.edu/trmm/data/document/GPM_database_description_1.0_201601.pdf.Liu, C., & Zipser, E. J. (2015). The global distribution of largest, deepest, and most

intense precipitation systems. *Geophysical Research Letters*, **42**, 3591–3595, https://doi.org/10.1002/2015GL063776.Liu, C., Zipser, E. J., Cecil, D. J., Nesbitt, S. W., & Sherwood, S. (2008). A cloud and precipitation feature database from nine years of TRMM observations. *Journal of Applied Meteorology and Climatology*, **47**, 2712–2728, https://doi.org/10.1175/2008JAMC1890.1.Liu, C., Cecil, D. J., & Zipser, E. J. (2011). Relationships between lightning flash rates and passive microwave brightness temperatures at 85 and 37 GHz over the tropics and subtropics. *Journal of Geophysical Research*, **116**, 1–14, https://doi.org/10.1029/2011JD016463.Liu, C., Cecil, D. J., Zipser, E. J., Kronfeld, K., & Robertson, R. (2012). Relationships between lightning flash rates and radar reflectivity vertical structures in thunderstorms over the tropics and subtropics. *Journal of Geophysical Research*, **117**, 1–19, https://doi.org/10.1029/2011JD017123.Mach, D. M. (2020). Geostationary Lightning Mapper Clustering Algorithm Stability. *Journal of Geophysical Research: Atmospheres*, **125**, 1–14, https://doi.org/10.1029/2019JD031900.Makowski, J. A., Macgorman, D. R., Biggerstaff, M. I., & Beasley, W. H. (2013). Total lightning characteristics relative to radar and satellite observations of Oklahoma Mesoscale Convective Systems. *Monthly Weather Review*, **141**, 1593–1611, https://doi.org/10.1175/MWR-D-11-00268.1.Marchand, M., Hilburn, K. A., & Miller, S. D. (2019). Geostationary Lightning Mapper and Earth Networks Lightning detection over the contiguous United States and dependence on flash characteristics. *Journal of Geophysical Research: Atmospheres*, **124**, 11552–11567, https://doi.org/10.1029/2019JD031039.Matsui, T., Chern, J. D., Tao, W. K., Lang, S., Satoh, M., Hashino, T., & Kubota, T. (2016). On the land-ocean contrast of tropical convection and microphysics statistics derived from TRMM satellite signals and global storm-resolving models. *Journal of Hydrometeorology*, **17**, 1425–1445, https://doi.org/10.1175/JHM-D-15-0111.1.Matthee, R., Mecikalski, J. R., Carey, L. D., & Bitzer, P. M. (2014). Quantitative differences between lightning and nonlightning convective rainfall events as observed with polarimetric radar and MSG satellite data. *Monthly Weather Review*, **142**, 3651–3665, https://doi.org/10.1175/MWR-D-14-00047.1.May, R. M., Arms, S., Marsh, C. P., Bruning, E. C., Lee, J. R., Goebbert, K., et al. (2021). MetPy: A Python package for meteorological data. https://doi.org/10.5065/D6WW7G29.Medina, B. L., Carey, L. D., Lang, T. J., Bitzer, P. M., Deierling, W., & Zhu, Y. (2021). Characterizing charge structure in central Argentina thunderstorms during RELAMPAGO utilizing a new charge layer polarity identification method. *Earth and Space Science*, **8**, https://doi.org/10.1029/2021EA001803.Murphy, M. J., & Said, R. K. (2020). Comparisons of lightning rates and properties from the U.S. National Lightning Detection Network (NLDN) and GLD360 with GOES-16 Geostationary Lightning Mapper and Advanced Baseline Imager data. *Journal of Geophysical Research: Atmospheres*, **125**, https://doi.org/10.1029/2019JD031172.Murugavel, P., Pawar, S. D., & Gopalakrishan, V. (2014). Climatology of lightning over Indian region and its relationship with convective available potential energy. *International Journal*

of Climatology, **34**, 3179–3187, https://doi.org/10.1002/joc.3901.Nesbitt, S. W., Zipser, E. J., & Cecil, D. J. (2000). A census of precipitation features in the tropics using TRMM: radar, ice scattering, and lightning observations. *Journal of Climate*, **13**, 4087–4106, https://doi.org/10.1175/1520-0442(2000)013<4087:ACOPFI>2.0.CO;2.Orville, R. E. (1990): Winter lightning along the east coast. *Geophysical Research Letters*, **17**, 713–715, https://doi.org/10.1029/GL017i006p00713.Orville, R. E., & Henderson, R. W. (1986). Global distribution of midnight lightning: September 1977 to August 1978. *Mon. Weather Rev.*, **114**, 2640–2653, https://doi.org/10.1175/1520-0493(1986)114<2640:GDOMLS>2.0.CO;2.Orville, R. E., & Huffines,G. R. (2001). Cloud-to-ground lightning in the United States: NLDN results in the first decade, 1989-98. *Monthly Weather Review*, **129**, 1179–1193, https://doi.org/10.1175/1520-0493(2001)129<1179:CTGLIT>2.0.CO;2.Petersen, W. A., & Rutledge, S. A. (2001). Regional variability in tropical convection: Observations from TRMM. *Journal of Climate*, **14**, 3566–3586, https://doi.org/10.1175/1520-0442(2001)014<3566:RVITCO>2.0.CO;2.Petersen, W. A., H. J. Christian, & S. A. Rutledge (2005). TRMM observations of the global relationship between ice water content and lightning. *Geophysical Research Letters*, **32**, 1–4, https://doi.org/10.1029/2005GL023236.Price, C., & Rind, D. (1992). A simple lightning parameterization for calculating global lightning distributions. *Journal of Geophysical Research*, **97**, 9919–9933, https://doi.org/10.1029/92JD00719.Rudlosky, S. D., & Fuelberg, H. E. (2013). Documenting storm severity in the Mid-Atlantic region using lightning and radar information. *Monthly Weather Review*, **141**, 3186–3202, https://doi.org/10.1175/MWR-D-12-00287.1.Rudlosky, S. D., & Virts, K. S. (2021). Dual Geostationary Lightning Mapper observations. *Monthly Weather Review*, **149**, 979–998, https://doi.org/10.1175/mwr-d-20-0242.1.Rudlosky, S. D., Goodman, S. J., Virts, K. S., & Bruning, E. C. (2019): Initial Geostationary Lightning Mapper observations. *Geophysical Research Letters*, 1097–1104, https://doi.org/10.1029/2018GL081052.Rutledge, S. A., Williams, E. R., & Keenan, T. D. (1992). The Down Under Doppler and Electricity Experiment (DUNDEE): Overview and preliminary results. *Bulletin of the American Meteorological Society*, **73**, 3–16, https://doi.org/10.1175/1520-0477(1992)073<0003:TDUDAE>2.0.CO;2.Rutledge, S. A., Hilburn, K. A., Clayton, Fuchs, A. B. R., & Miller, S. D. (2020). Evaluating Geostationary Lightning Mapper flash rates within intense convective storms. *Journal of Geophysical Research: Atmospheres*, **125**, 1–16, https://doi.org/10.1029/2020JD032827.Saunders, C. P. R. (1993). A review of thunderstorm electrification processes. *Journal of Applied Meteorology*, **32**, 642–655, https://doi.org/10.1175/1520-0450(1993)032<0642:AROTEP>2.0.CO;2.(2009). Preliminary development and evaluation of lightning jump algorithms for the real-time detection of severe weather. *Journal of Applied Meteorology and Climatology*, **48**, 2543–2563, https://doi.org/10.1175/2009JAMC2237.1.Schultz, C. J., Petersen, W. A., & Carey, L. D. (2011). Lightning and severe weather: A comparison between total and cloud-to-ground lightning trends. *Weather and Forecasting*, **26**, 744–755, https://doi.org/10.1175/WAF-D-

10-05026.1.Spencer, R. W., Goodman, H. M. & Hood, R. E. (1989). Precipitation retrieval over land and ocean with the SSM/I: Identification and characteristics of the scattering signal. *Journal of Atmospheric and Ocean Technology*, **6**, 254–273, https://doi.org/10.1175/1520-0426(1989)006<0254:PROLAO>2.0.CO;2.Tao, W. K., Smith, E. A., Adler, R. F., Haddad, Z. S., Hou, A. Y., Iguchi, T., et al. (2006). Retrieval of latent heating from TRMM measurements. *Bull. Am. Meteorol. Soc.*, **87**, 1555–1572, https://doi.org/10.1175/BAMS-87-11-1555.Thompson, R. L., Edwards, R., Hart, J. A., Elmore, K. L., & Markowski, P. (2003). Close proximity soundings within supercell environments obtained from the Rapid Update Cycle. *Weather and Forecasting*, **18**, 1243–1261, https://doi.org/10.1175/1520-0434(2003)018<1243:CPSWSE>2.0.CO;2.Tinmaker, M. I. R., Aslam, M. Y., & Chate, D. M. (2015). Lightning activity and its association with rainfall and convective available potential energy over Maharashtra, India. *Natural Hazards*, **77**, 293–304, https://doi.org/10.1007/s11069-015-1589-x.Toracinta, E. R., Cecil, D. J., Zipser, E. J., & Nesbitt, S. W. (2002). Radar, passive microwave, and lightning characteristics of precipitating systems in the tropics. *Monthly Weather Review*, **130**, 802–824, https://doi.org/10.1175/1520-0493(2002)130<0802:RPMALC>2.0.CO;2.Virts, K. S., Wallace, J. M., Hutchings, M. L., & Holzworth, R. H. (2015). Diurnal and seasonal lightning variability over the Gulf Stream and the Gulf of Mexico*. *Journal of the Atmospheric Sciences*, **72**, 2657–2665, https://doi.org/10.1175/JAS-D-14-0233.1.Weisman, M. L., & Klemp, J. B. (1982). The dependence of numerically simulated convective storms on vertical wind shear and buoyancy. *Monthly Weather Review*, **110**, 504–520, https://doi.org/10.1175/1520-0493(1982)110<0504:TDONSC>2.0.CO;2.Wilheit, T. T., Chang, A. T. C., King, J. L., Rodgers, E. B., Nieman, R. A., Krupp, B. M., et al. (1982).: Microwave radiometric observations near 19.35, 92, and 183 GHz of precipitation in Tropical Storm Cora. *Journal of Applied Meteorology*, **21**, https://doi.org/10.1175/1520-0450(1982)021<1137:MRONAG>2.0.CO;2.Williams, E. R., & Stanfill, S. 2002: The physical origin of the land – ocean contrast in lightning activity. *C. R. Physique*, **3**, 1277–1292, https://doi.org/10.1016/S1631-0705(02)01407-X.Workman, E. J., & Reynolds, S. E. (1949). Electrical activity as related to thunderstorm cell growth. *Bulletin of the American Meteorological Society*, **30**, 142–144.Wu, R., & Weinman, J. A. (1984) Microwave radiances from precipitating clouds containing aspherical ice, combined phase, and liquid hydrometeors. *Journal of Geophysical Research*, **89**, 7170–7178, https://doi.org/10.1029/JD089iD05p07170.Zajac, B. A., & Rutledge, S. A. (2001). Cloud-to-ground lightning activity in the contiguous United States from 1995 to 1999. *Monthly Weather Review*, **129**, 999–1019, https://doi.org/10.1175/1520-0493(2001)129<0999:CTGLAI>2.0.CO;2.Zhang, D., & Cummins, K. L. (2020). Time evolution of satellite-based optical properties in lightning flashes, and its impact on GLM flash detection. *Journal of Geophysical Research: Atmospheres*, **125**, https://doi.org/10.1029/2019JD032024.Zheng, D., Zhang, Y., Meng, Q., Chen, L., & Dan, J. (2016). Climatology of lightning activity in South China and its relationships to precipitation and

convective available potential energy. *Advances in Atmospheric Sciences*, **33**, 365–376, https://doi.org/10.1007/s00376-015-5124-5.Zipser, E. J., & Lutz, K. R. (1994). The vertical profile of radar reflectivity of convective cells: A strong indicator of storm intensity and lightning probability? *Monthly Weather Review*, **122**, 1751–1759, https://doi.org/10.1175/1520-0493(1994)122<1751:TVPORR>2.0.CO;2.Zipser, E. J., Cecil, D. J., & Liu, C. (2006). Where are the most intense thunderstorms on Earth? *Bulletin of the American Meteorological Society*, 1057–1072, https://doi.org/10.1175/BAMS-87-8-I057.Zuluaga, M. D., & Houze Jr., R. A. (2015). Extreme convection of the near-equatorial Americas, Africa, and adjoining oceans as seen by TRMM. *Monthly Weather Review*, **143**, 298–316, https://doi.org/10.1175/MWR-D-14-00109.1.